Solvent volume-driven $CuInAlS_2$ nanoflake counter electrode for effective electrocatalytic tri-iodide reduction in dye-sensitized solar cells

C. Ravi Dhas[1*], A. Jennifer Christy[1], R.Venkatesh[1], Subhendu K. Panda[2], B. Subramanian[2], K.Ravichandran[3], P.Sudhagar[4], A. Moses Ezhil Raj[5]

[1]PG & Research Department of Physics, Bishop Heber College (Autonomous), Tiruchirappalli-620 017, Tamil Nadu, India

[2]CSIR-Central Electrochemical Research Institute (CECRI), Karaikudi-630 006, India

[3]Department of Physics, AVVM Sri Pushpam College, (Autonomous), Poondi, Thanjavur-613 503, Tamil Nadu, India.

[4]Photocatalyst and Coatings Group, SPECIFIC, College of Engineering, Swansea University (Bay Campus), Fabianway, Swansea SA1 8EN, United Kingdom

[5]Department of Physics, Scott Christian College, (Autonomous), Nagercoil-629 003, Tamil Nadu, India

*Corresponding author email address: ravidhasc@gmail.com

Corresponding Author

Dr. C. Ravi Dhas
Head and Assistant Professor,
PG & Research Department of Physics,
Bishop Heber College (Autonomous),
Tiruchirappalli-620 017,
Tamil Nadu, India.
Mobile: +91 9443076209
Land line: 0431-2770136
Fax: 0431-2770293
e-mail: ravidhasc@gmail.com; cravidhas@gmail.com

Abstract

The influence of solvent volume on the properties of $CuInAlS_2$ (CIAS) thin films deposited using simple and cost-effective nebulizer spray technique is studied. The polycrystalline CIAS thin films with tetragonal structure have been observed from the XRD results. SEM images show nanoflake-like structure on the film surface. The elemental presence and its chemical composition were examined by XPS and EDS. The deposited CIAS film for different solvent volume exhibited p-type semiconductor. Cyclic voltammetry, electrochemical impedance spectroscopy and Tafel polarization measurements demonstrated that CIAS counter electrodes are capable of tri-iodide reduction process. The performances of photocurrent density-voltage for the CIAS CE exhibited the maximum efficiency of 2.55% with the short-circuit current density of 7.22 mA cm^{-2}.

Key words: CIAS, nebulizer spray, thickness, counter electrode, dye-sensitized solar cells.

1. Introduction

The energy crisis is the major problem in the current trend of the world. In recent years, the active research area in the field of energy is the solar energy owing to a clean and sustainable energy. Dye-sensitized solar cells (DSSCs) are the next generation of solar cells since they were first reported by Gratzel's group in 1991 due to its low-cost, ease production, environmental friendliness, and high efficiency [1, 2]. The major components of DSSCs are the semiconducting material with sensitizer dye as the working electrode, the redox electrolyte and the counter electrode. A better alternative for these components has been tested due to its cost effective and the better outcome of efficiency [3]. TiO_2 is an earth-abundant and non-toxic material and widely used as the working electrode due to its electron mobility and stability towards dyes [4]. Still research is being carried out on the synthesize of TiO_2 with different morphology, specific surface facets and a high surface area to improve

the efficiency in DSSCs [5, 6]. The effective dye-sensitizer in DSSC is Ruthenium which yielded an efficiency of about 11% [7]. The counter electrode also plays a crucial role in analyzing the efficiency of this family of excitonic solar cells. Generally, platinum (Pt) is used as the counter electrode (CE) prepared by thermal decomposition, chemical reduction, sputtering, etc [8-10]. The low earth abundant and expensive Pt CE which acts as a catalyst for the charge transfer reaction in the tri-iodide process has to be replaced with the low-cost and earth abundant materials [11]. Inorganic materials like sulfides, nitrides, carbides, carbon based materials, polymeric materials, etc are extensively utilized as the counter electrode in DSSCs [12, 13].

Chalcopyrite semiconductor I-III-VI_2 has attracted more attention towards the solar cell technologies. The non-toxic $CuInS_2$ semiconductor material, used as an absorber layer in heterojunction solar cells has a high absorption coefficient ($> 10^4$ cm^{-1}) with the optical band gap value varying from 1.39-1.55 eV which depends upon the deposition techniques and growth conditions [14]. Few reports are available on $CuInS_2$ and $CuInGaS_2$ as the CE in DSSCs to the best of our knowledge [15-17]. Since Ga is a rare and costly element, it can be either substituted by earth abundant and non toxic elements such as Al, Fe, Ce, Sn, Zn, Na, etc in $CuInS_2$ [18-23]. The ternary $CuAlS_2$ is also a p-type material with the optical band gap of 3.4 eV. The structure of $CuAlS_2$ is similar to that of $CuInS_2$ with wide ranging properties, good thermal stability and it can be readily adopted for chalcogenide solar cells [24]. Among various chemical and physical deposition techniques [25, 26], nebulizer spray route is low-cost and versatile technique which can produce fine micron size droplets and can produce device quality films [17, 27]. The thickness of the counter electrode layer needs to be optimized for better performance of DSSCs as it can alter the morphology and electronic structure of a material. Also, the amount of deposit has a key role in electrocatalytic tri-iodide reduction and charge collection from the external circuit [28]. In the present work, $CuInAlS_2$

(CIAS) was deposited by nebulizer spray technique for the first time using different solvent volumes. The obtained CIAS films were used as counter electrodes in assembled DSSCs. The structural, elemental analysis, electrical, optical, electrochemical and photovoltaic performances on CIAS thin films are discussed in detail.

2. Experimental

2.1. Preparation of CIAS thin film

CIAS thin films were deposited at a constant substrate temperature of 300 °C for different solvent volumes (10, 30, 50 and 70 ml). The solution was prepared by taking Copper (II) chloride dihydrate ($CuCl_2.2H_2O$), indium (III) chloride ($InCl_3$, anhydrous), aluminum (III) chloride ($AlCl_3$, anhydrous) and thiourea ($SC(NH_2)_2$) with the molar ratio of 1:0.7:0.3:4 and dissolved in distilled water vigorously at room temperature. The chemicals used in this process were purchased from Alfa Aesar (AR grade). The prepared solution was sprayed onto clean glass and FTO substrates with the pressure of 1.0 kg cm^{-2} to produce device quality CIAS thin films.

2.2. Fabrication of DSSCs device

All the assembled DSSCs were fabricated based on standard procedure using TiO_2 photoanode for a fair comparison. FTO substrates were ultrasonically cleaned in ethanol, acetone and deionized water for 10 minutes to remove the contaminants from the surface. The cleaned FTO substrate was immersed in 20 mM aqueous solution of $TiCl_4$ to form TiO_2 blocking layer. The resultant film was gradually heated in air at 450 °C for 30 minutes. Commercial TiO_2 paste (Degussa P25 TiO_2 Purchased from Sigma Aldrich) was doctor bladed over blocking layer to obtain mesoporous and scattering layer which was baked at 150 °C for 5 minutes and finally annealed in air at 500 °C for 1 hour respectively. The

obtained TiO_2 photoanode was soaked in a solution of N719 dye mixed with 0.3 mM of ethanolic solution for 12 hours at room temperature under dark condition. The excess dye molecules over TiO_2 photoanode were removed by dipping in ethanol and allowed to dry. The platinum CE layer on FTO was prepared by spin coating, the solution of $H_2PtCl_6.6H_2O$ dispersed in 10 mM isopropanol solution annealed at 400 °C for 30 minutes. The nebulizer-spray deposited CIAS/FTO CEs and Pt CE were separated using a surlyn film spacer with dye-sensitized TiO_2 electrode. The iodine electrolyte solution containing 0.06 M LiI, 0.6 M 1-propyl-2,3-dimethylimidazolium iodide, 0.03 M I_2, 0.5 M 4-tertbuyl pyridine and 0.1 M guanidinium thiocyanate dissolved in acetonitrile was injected in the gap between the two electrodes with a small capillary syringe and the holes were completely sealed with molten glue. The active area of the fabricated DSSCs was 0.4×0.4 cm^2.

2.3. Characterization

The crystal structure of the films was analyzed with a PANanalytical X'PERT PRO diffractometer by Cu K_α radiation with a wavelength of 1.5406 Å. Raman traces were recorded using Reinshaw (Invia Make) spectrometer by employing Ar^+ ion laser (514 nm). The surface properties of the films were analyzed by scanning Electron Microscope (VEGA3 TESCAN) and Atomic Force Microscope (A100, APE Research). X-ray photoelectron spectrometer (Kratos axis ultra DLD) and energy dispersive spectroscopy (Bruker) were utilized to investigate the chemical state of the elements present in CIAS thin film and its composition. The optical absorbance of the CIAS films was recorded by JASCO UV-Vis-NIR-V-670 Spectrophotometer. The electrical properties of CIAS films were determined by four probe method with the Keithley 2400 source meter and Ecopia HMS-3000 source meter, respectively. The photovoltaic performance of the assembled DSSCs was studied using a potentiostat (VMP3, BIO-LOGIC) under constant illumination from a solar simulator

(Photoemission Tech) equipped with an AM 1.5G filter set. The output intensity of the light source was kept constant (100 mW cm^{-2}). Cyclic voltammetric measurements were recorded using three electrode cell configurations. Pt wire was used as a counter electrode, iodine solution (10 mM LiI, 1mM I_2, and 0.1 M $LiClO_4$) as an electrolyte, CIAS/FTO films as working electrode and standard calomel electrode (SCE) served as the reference electrode. The electrochemical impedance spectroscopy (EIS) of the counter electrode was evaluated at the constant dc potential of 0.7 V under dark condition in the frequency range 0.1 Hz to 1 MHz with an amplitude voltage of 10 mV.

3. Results and discussion

3.1. Thickness measurement

The thickness measurement of CIAS thin films was examined by stylus profilometer and found it to be varying between 350 and 1250 nm as a function of solvent volume (Fig.1). The thickness of CIAS film increased progressively upto 50 ml solvent volume and decreased at higher solvent volume (70 ml). The increase in solvent volume might provide longer time deposition for the ions to settle over the substrate and slow cooling rate of deposits onto the film surface might lead to increment in film thickness [29]. The thickness of the film was not exactly proportional to the solvent volume due to an inadequate supply of thermal energy to decompose the precursors completely resulting in the formation of the powdery film at higher solvent volume [30].

3.2. Structural analysis

Figure 2 depicts the XRD patterns of CIAS thin films deposited using different solvent volumes. The deposited CIAS thin films are polycrystalline in nature with the tetragonal structure as compared to the standard JCPDS card no 65-1572 of chalcopyrite

$CuInS_2$. The diffraction peaks present at 2θ = 27.9°, 46.9°, 55.5° are assigned to (1 1 2), (2 0 4), and (2 1 5) planes respectively. The crystalline nature of CIAS thin film mainly depends upon the solvent volume. The intensity of the peaks ameliorates with the increasing solvent volume upto 50 ml and deteriorates for the higher solvent volume 70 ml. The enhancement of preferential orientation plane (1 1 2) could be due to the growth of grains at low energy surface sites with an increase in film thickness [31]. The decline in the peak intensity at higher solvent volume 70 ml might be attributed to the poor thermal decomposition of the precursor as more amount of atomic species impinged over the substrate [32].

The crystallite size (*D*) of the CIAS thin films for the predominant plane (1 1 2) was determined from Scherrer formula [33]

$$D = \frac{K\,\lambda}{\beta \cos\theta} \quad \text{(nm)} \qquad (1)$$

where '*K*' = 0.9 is the shape factor, 'λ' is the wavelength of X-ray (Kα=1.5406 Å), 'β' is the full-width half maximum (FWHM), 'θ' is the diffraction angle. The microstrain (ε), dislocation density (δ) and lattice parameters of the CIAS thin films were calculated from the following relations [17],

$$\varepsilon = \frac{\beta \cos\theta}{4} \qquad (2)$$

$$\delta = \frac{1}{D^2} \qquad (3)$$

$$\frac{1}{d_{hkl}^2} = \frac{h^2 + k^2}{a^2} + \frac{l^2}{c^2} \qquad (4)$$

Figure 3 (i) clearly depict the increment in crystallite size and corresponding decrement in microstrain and dislocation density with the increase in film thickness. The nucleation and grain growth process in the formation of thin film essentially depend on the density of atomic species in the solution [34]. The preferentially oriented plane (1 1 2) attains the maximum intensity for the CIAS film deposited by 50 ml with reduced FWHM and larger crystallite size. Moreover, the microstrain and dislocation density decreases to large extent for the CIAS film prepared by 50 ml and insists that the decrease in the concentration of lattice imperfections, and better crystalline quality of CIAS thin film are highly beneficial to counter electrode in DSSCs [35]. The decrease in crystallite size value at the higher solvent volume 70 ml is due to the arrangement of new smaller grains on the bigger grains [36]. The calculated lattice parameters (‘*a*’ & ‘*c*’) for all the films are presented in Table 1. The tetragonal distortion and full width at half maximum (FWHM) for CIAS films as a function of solvent volume are shown in Figure 3 (ii). The c/a ratio values gradually increase with solvent volume suggesting that not much distortion takes place whereas extreme variation in FWHM shows that crystallite growth depends on solvent volume.

3.3. Raman spectra

Raman spectroscopy provides details about phase identification, presence of secondary phases, crystalline quality, bond strength and chemical environment of cations [31]. Raman spectra of CIAS thin films for different solvent volumes are shown in Fig.4. The broad peak centered around 290 – 305 cm^{-1} corresponds to A1 mode and no other peaks related to B_2 and E mode were observed. Absence of secondary phases indicates the phase purity of the prepared films. It is well known that $CuInS_2$ thin film usually grows with the mixed phase of chalcopyrite (CH) ordering and Cu-Au (CA) ordering [37], where the A1 peak of CH and CA ordering is situated at 290 and 305 cm^{-1} respectively. The FWHM of A1

mode was estimated for all the deposited CIAS thin films and found to be 72, 66, 63 and 65 cm^{-1} prepared for different solvent volumes 10, 30, 50 and 70 ml respectively. The least value of FWHM obtained for the film deposited by 50 ml solvent volume indicates better crystalline quality as evident from XRD results and could be due to the phonon confinement in the lattice [38].

3.4. Scanning Electron Microscopy (SEM)

SEM images of CIAS thin film deposited for different solvent volumes are shown in Fig. 5. The small spherical grains with needle-like structure initially began to grow in the lower solvent volume 10 ml due to a poor crystalline growth of CIAS film on the substrate. As the volume of solution was increased to 30 ml, nanosheets were observed indicating the improvement in the crystalline quality of the film as evident from XRD, the peak intensity of (1 1 2) plane increasing with the increasing solvent volume. The nanosheets turned into nanoflake morphology for the CIAS film prepared using 50 ml solvent volume. This type of conversion occurs in chalcopyrite films due to the concentration of thiourea (sulfur source) which is not only a precursor but also a morphological directing agent. The plane view of CIAS film indicates that grains are packed densely with high surface area. The nanoflake interconnected network morphology is highly beneficial to electrocatalytic activity as it will accommodate more electrolyte species and fast reduction rate of I_3^- is possible [39]. The spherical grains agglomerated were observed due to coalescence process for the film deposited using higher solvent volume 70 ml of CIAS film.

3.5. Atomic force microscope (AFM)

AFM images of 2D and 3D for CIAS thin films prepared for different solvent volumes are shown in Fig. 6. Generally, nucleation, crystal growth and grain growth are the

various stages of the film growth. The nuclei were grown randomly over the film surface for lower thickness of the deposited CIAS film which exhibited larger surface roughness. The increase in the solvent volume led the grains to be coalesced and develop in a particular direction to reduce the energy of the substrate-film interface and free surface energy [40]. The surface roughness of the CIAS thin films decreased with the increasing solvent volume upto 50 ml (Table 1) and increased at the higher solvent volume 70 ml due to large number of agglomerated grains [41]. The better results can be attained for the minimum surface roughness of the CIAS film deposited using 50 ml.

3.6. X-ray photoelectron spectroscopy (XPS)

Figure 7 (i) shows the XPS survey spectrum of CIAS thin film deposited by 50 ml solvent volume in a wide energy range of 0 – 1200 eV. The characteristic peaks of Cu 2p, In 3p, O 1s, In 3d, C 1s, S 2p, Al 2s, Al 2p, and S 3s were observed in survey spectra confirming the presence of elements in CIAS film. The obtained binding energy values of Cu, In, Al and S are reported in the literature [42]. The binding energy of carbon species C 1s (284.1 eV) was utilized to calibrate the spectra.

The core level spectra of copper, indium, aluminium and sulfur of CIAS thin film are displayed in Fig. 7 (ii). The binding energy of copper peaks 931.2 and 950.0 eV corresponding to $2p_{3/2}$ and $2p_{1/2}$ respectively was split by 19.8 eV representing the Cu (I) oxidation state. Perera et al. reported a satellite peak at 942 eV that denotes Cu (II) oxidation state of $2p_{3/2}$ [43]. The nebulizer spray-coated CIAS thin film clearly represented the absence of Cu (II) state and confirmed the Cu (I) state. The indium peak $3d_{5/2}$ and $3d_{3/2}$ emerged at 444.5 and 452.1 eV with the splitting binding energy of 7.6 eV. A peak at 74.07 and 160.0 eV indicates Al 2p and S $2p_{3/2}$. The presence of oxygen (531.1 eV) and sulfur (167.8 eV) peaks were owing to the formation of sulphate as surface contaminant [44].

3.7. Energy dispersive X-ray analysis (EDS)

The EDS spectrum of CIAS thin film deposited by 50 ml solvent volume is shown in Fig. 8. Copper, indium, aluminium and sulfur were the only elements present in the prepared CIAS thin film. The inset of table in Fig. 8 indicates that the films with better stoichiometric ratio were obtained using different solvent volumes.

3.8. Optical properties

The absorption spectra of CIAS thin film deposited for different solvent volumes were recorded in the wavelength region of 350 – 1100 nm as shown in Fig. 9. The absorption spectra of CIAS thin film increased gradually in the visible region as the thickness of the film increased. The maximum absorbance was observed for the CIAS film deposited using 50 ml solvent volume. Wide absorption spectra in the visible region are highly suitable for the solar cell device applications.

The optical band gap energy of the CIAS thin film prepared for different solvent volumes can be determined using the Tauc plot relation [33],

$$\alpha h\nu = A\left(h\nu - E_g\right)^n \qquad (5)$$

where 'α', '$h\nu$', 'E_g' and 'n' are absorption co-efficient, incident photon energy, band gap and type of transition. The value of n=1/2, since CIAS is a direct band gap semiconducting material [45]. The optical energy band gap values of the deposited CIAS films (Fig.10) were estimated using Tauc plot and found to be 1.37, 1.33, 1.27 and 1.25 eV. The variation in the band gap value could be attributed to the change in carrier concentration [46]. There are some more reasons for the change in the band gap values such as quantum confinement effect, coulomb interaction within the conduction band which leads to shrinkage

and renormalization of band gap, electron-electron interaction, etc., as reported by many researchers [47, 48].

3.9. Electrical properties

Electrical properties of the counter electrode layers are most important for better charge collection from external circuit and in fast reduction of I_3^- species in DSSCs. The electrical parameters such as resistivity (ρ), carrier concentration (n) and Hall mobility (μ) of CIAS films were determined from Hall measurements and thermal activation energy values were estimated from linear four probe method. Hall effect measurement shows that all the CIAS films deposited were p-type conductivity in nature. The obtained electrical parameters were represented as a function of solvent volume which is shown in Fig. 11. The resistivity values lie in the range between 2.836 and 5786 Ω cm and carrier concentration and mobility values lies from 4×10^{12} to 2.97×10^{17} cm^{-3} and 7.42 to 267 $cm^2\ V^{-1}\ s^{-1}$. The obtained electrical parameters are consistent with the previous values of thermally evaporated CIAS films [49]. The resistivity values markedly decreased with the increase in solvent volume and the corresponding changes in carrier density and hall mobility were observed.

Figure 12 shows the Arrhenius behaviour (ln σ vs $1000/T$ (K^{-1})) of CIAS films for different solvent volumes. The activation energy values estimated from the plots are given in Table 1. The resistivity variation observed in CIAS thin films depends upon number of grain boundaries. Moreover, one could observe from the Arrhenius plot that there is a minor dependence of temperature over the conductivity of CIAS films. The main phenomena affecting the charge transport in semiconductor thin films are scattering centers which could be classified into three different types: (i) grain boundary scattering, (ii) scattering due to impurity/defect centers and (iii) scattering due to lattice vibrations or phonons [50]. The grain boundary scattering plays a major part which reduces the mean free path of the charge

carriers in polycrystalline semiconductor films [51]. The CIAS film prepared at 50 ml solvent volume has considerable resistivity (2.836 Ω cm), hole mobility (7.42 $cm^2 V^{-1} s^{-1}$), and carrier concentration (2.97×10^{17} cm^{-3}) due to the preferential orientation of (1 1 2) plane and can function efficiently as the CE in DSSCs.

3.10. Electrochemical activity and stability of CEs

The electrocatalytic activity of CIAS counter electrodes towards the tri-iodide process in the electrolyte strongly impacts the device performances [52]. The catalytic behaviour of CIAS counter electrode towards the tri-iodide process was investigated by cyclic voltammograms (CV) in iodine electrolyte (Fig. 13 (i)).

The electrocatalytic activity of CIAS films has shown a significant improvement with the increase in solvent volume. The poor interactions of the redox species in the electrolyte lead to an increase in interfacial charge transfer certainly results in poor fill factor (Table 3) for CIAS CEs prepared using 10 and 30 ml assembled DSSCs [53]. The oxidation and reduction reactions involved in the CE/electrolyte interface are given by

$$3I^- \leftrightarrow I_3^- + 2e^- \qquad (6)$$

The two vital parameters of electrocatalytic activity are anodic (J_{pa}) and cathodic (J_{pc}) current densities and peak-to-peak separation (ΔE_P). Generally, ΔE_P varies inversely with the charge transfer rate from the reaction kinetics, denoting that the lower ΔE_P promotes the higher electrocatalytic activity [28]. ΔE_P can be determined by the following relation:

$$\Delta E_P = E_{pc} - E_{pa} \qquad (7)$$

The cathodic current density increased progressively with the increasing film thickness and decreased the peak-to-peak separation. The highest J_{pc} was achieved for the CIAS CE prepared using 50 ml solvent volume with the lowest ΔE_P compared to other CIAS CEs. The better crystalline quality of the CIAS film with lower resistivity promotes fast

charge transfer kinetics [54]. The stability of the CIAS CE deposited using 50 ml solvent volume was evaluated in the redox species (I^-/I_3^-) at a scanning rate of 50 mV/s. Figure 13 (ii) clearly depicts that no changes in current densities after 40 cycles continuously indicate good stability of the CIAS CE in iodine electrolyte.

3.11. Electrochemical Impedance Spectroscopy (EIS)

The EIS measurements were carried out to study the electrochemical behaviour of the CIAS CEs. EIS analysis was performed for the CIAS CEs with the TiO_2 based-DSSCs devices and the obtained Nyquist Plots are shown in Fig. 14 (i). The inset of Fig. 14 (i) represents the equivalent circuit of the CIAS CEs fitted by ZsimpWin software. The series resistance (R_s) signifies the intercept on the real axis at high frequency. The semicircle in the high frequency range denotes the charge transfer resistance (R_{ct}) [55]. Notably, the small value of R_{ct} causes higher electrocatlytic activity in the tri-iodide species [56]. The values of R_s and R_{ct} are listed in Table 2. It is obvious that R_s and R_{ct} deteriorated with the increasing film thickness. The lowest R_s and R_{ct} attained for the CIAS CE deposited using 50 ml solvent volume are associated with the lower resistivity and enhance the efficiency in DSSCs.

3.12. Tafel Analysis

Figure 14 (ii) shows the symmetric cells of CIAS CEs to analyze the interfacial charge transfer. The Tafel curve is a plot between the logarithmic current density and applied voltage. The exchange current density (J_0) and the limiting diffusion current density (J_{lim}) can be determined from the intermediate potential and a high potential respectively [28]. The value of J_{lim} estimated for CIAS CEs is displayed in Table 2. The exchange current density J_0 and limiting diffusion coefficient J_{lim} attained for the CIAS CE prepared using 50 ml solvent

volume were comparable to Pt CE which indicates that CIAS CE can be utilised instead of Pt in DSSCs.

3.13. Photocurrent density-voltage (J-V) characterization

DSSC fabricated with CIAS CE prepared for different solvent volumes is examined to find an alternative Pt CE. The current density-voltage curve of Pt and CIAS CEs are depicted in Fig. 15. The obtained values of short-circuit current density (J_{sc}), open-circuit voltage (V_{oc}), fill factor (*FF*) and efficiency (η) for Pt and CIAS CEs are listed in Table 3. The increment in the efficiency of CIAS CEs with the film thickness was observed. The energy difference between the quasi Fermi level of the electrons in the photoanode under illumination and the redox potential of the redox species (I^-/I_3^-) electrolyte is the reason for the similar V_{oc} in the counter electrode [57]. As the lower solvent volumes possessed poor catalytic activity, the lowest fill factor was attained. The maximum J_{sc} (7.22 mA cm^{-2}) was achieved with the highest efficiency of 2.55% for the CIAS CE coated using the solvent volume 50 ml. The high R_s and R_{ct} obtained from EIS spectra at the higher solvent volume 70 ml led to the decrement in *FF* (0.42) and efficiency (2.12%).

4. Conclusion

Quaternary chalcopyrite CIAS thin films were successfully coated by simple and cost-effective nebulizer spray method for different solvent volumes. The effect of solvent volumes plays an important role in XRD, SEM, optical and electrical properties. The single phase $CuInAlS_2$ was achieved and confirmed by both XRD and Raman studies. Nano-flakes obtained at the higher film thickness provided the pathway for charge transfer and promoted high electrocatalytic activity. The lower resistivity with higher carrier concentration resulted in minimum charge transfer resistance from EIS analysis. Though the maximum efficiency

obtained for the optimized CIAS CE (2.55%) is quite low compared to the commercial Pt CE (5.30%), by altering the preparation conditions CIAS CE can replace Pt CE.

Acknowledgement

The authors would like to record their sincere thanks to the University Grants Commission, New Delhi for providing financial support through Major Research Project Scheme (MRP) [F.no.42-903/2013(SR)]. The authors also acknowledge Dr. R. Ramesh Babu, Assistant Professor, School of Physics, Bharathidasan University, Tiruchirappalli-24, for extending the Hall measurement facilities established under the DST grant (D.O.No.SR/S2/CMP-35/2004). One of the authors, Dr. S. K. Panda, would like to thank the Department of Science and Technology (DST), Government of India, for the financial support (Project no: SB/FT/CS-048/2012).

References

[1] Li L, Yang Y, Fan R, Jiang Y, Wei L, Shi Y, Yu J, Chen S, Wang P, Yang B (2014) A simple modification of near-infrared photon-to-electron response with fluorescence resonance energy transfer for dye-sensitized solar cells. J Power Sources 264:254-261.

[2] Gong F, Wang H, Xu X, Zhou G, Wang Z-S (2012) In situ growth of Co0. 85Se and Ni0. 85Se on conductive substrates as high-performance counter electrodes for dye-sensitized solar cells. J Am Chem Soc 134:10953-10958.

[3] Banerjee A, Upadhyay KK, Bhatnagar S, Tathavadekar M, Bansode U, Agarkar S, Ogale SB (2014) Nickel cobalt sulfide nanoneedle array as an effective alternative to Pt as a counter electrode in dye sensitized solar cells. RSC Adv 4:8289-8294.

[4] Chen X, Mao SS (2007) Titanium dioxide nanomaterials: synthesis, properties, modifications, and applications. Chem Rev 107:2891-2959.

[5] Sivaranjani K, Agarkar S, Ogale SB, Gopinath CS (2012) Toward a Quantitative Correlation between Microstructure and DSSC Efficiency: A Case Study of TiO2–x N x Nanoparticles in a Disordered Mesoporous Framework. J Phys Chem C 116:2581-2587.

[6] Sauvage F, Chen D, Comte P, Huang F, Heiniger L-P, Cheng Y-B, Caruso RA, Graetzel M (2010) Dye-sensitized solar cells employing a single film of mesoporous TiO2 beads achieve power conversion efficiencies over 10%. Acs Nano 4:4420-4425.

[7] Nazeeruddin MK, Kay A, Rodicio I, Humphry-Baker R, Müller E, Liska P, Vlachopoulos N, Grätzel M (1993) Conversion of light to electricity by cis-X2bis (2, 2'-bipyridyl-4, 4'-dicarboxylate) ruthenium (II) charge-transfer sensitizers (X= Cl-, Br-, I-, CN-, and SCN-) on nanocrystalline titanium dioxide electrodes. J Am Chem Soc 115:6382-6390.

[8] Papageorgiou N, Maier W, Grätzel M (1997) An iodine/triiodide reduction electrocatalyst for aqueous and organic media. J Electrochem Soc 144:876-884.

[9] Jun Y, Kim J, Kang MG (2007) A study of stainless steel-based dye-sensitized solar cells and modules. Sol Energy Mater Sol Cells 91:779-784.

[10] Ikegami M, Miyoshi K, Miyasaka T, Teshima K, Wei T, Wan C, Wang Y (2007) Platinum/titanium bilayer deposited on polymer film as efficient counter electrodes for plastic dye-sensitized solar cells. Appl Phys Lett 90:153122.

[11] Wu M, Ma T (2012) Platinum-Free Catalysts as Counter Electrodes in Dye-Sensitized Solar Cells. ChemSusChem 5:1343-1357.

[12] Wang L, Al-Mamun M, Liu P, Wang Y, Yang HG, Wang HF, Zhao H (2015) The search for efficient electrocatalysts as counter electrode materials for dye-sensitized solar cells: mechanistic study, material screening and experimental validation. NPG Asia Materials 7:e226.

[13] Mokurala K, Mallick S (2017) Effect of annealing atmosphere on quaternary chalcogenide-based counter electrodes in dye-sensitized solar cell performance: synthesis of Cu2FeSnS4 and Cu2CdSnS4 nanoparticles by thermal decomposition process. RSC Adv 7:15139-15148.

[14] Allouche NK, Jebbari N, Guasch C, Turki NK (2010) Influence of aluminum doping in CuInS 2 prepared by spray pyrolysis on different substrates. J Alloys Compd 501:85-88.

[15] Bhosale RK, Agarkar SA, Agrawal I, Naphade RA, Ogale S (2014) Nanophase CuInS 2 nanosheets/CuS composite grown by the SILAR method leads to high performance as a counter electrode in dye sensitized solar cells. RSC Adv 4:21989-21996.

[16] Chen B, Chang S, Li D, Chen L, Wang Y, Chen T, Zou B, Zhong H, Rogach AL (2015) Template synthesis of CuInS2 nanocrystals from In2S3 nanoplates and their application as counter electrodes in dye-sensitized solar cells. Chem Mater 27:5949-5956.

[17] Dhas CR, Christy AJ, Venkatesh R, Anuratha KS, Ravichandran K, Raj AME, Subramanian B, Panda SK (2017) Nebulizer spray-deposited CuInGaS2 thin films, a viable candidate for counter electrode in dye-sensitized solar cells. Sol Energy 157:58-70.

[18] Smaili F, Kanzari M, Rezig B (2008) Characterization of CuIn 1− x AlxS 2 thin films prepared by thermal evaporation. Mater Sci Eng C 28:954-958.

[19] Burnett JD, Gourdon O, Ranmohotti KG, Takas NJ, Djieutedjeu H, Poudeu PF, Aitken JA (2014) Structure–property relationships along the Fe-substituted CuInS 2 series: Tuning of thermoelectric and magnetic properties. Mater Chem Phys 147:17-27.
[20] Xiao L, Zhu J, Ding T, Wang Y, Fan Y, Bo Q (2015) Synthesis and characterization of Ce-incorporated CuInS 2 chalcopyrites. Mater Lett 159:392-394.
[21] Rabeh MB, Zribi M, Kanzari M, Rezig B (2005) Structural and optical characterization of Sn incorporation in CuInS 2 thin films grown by vacuum evaporation method. Mater Lett 59:3164-3168.
[22] Mahendran C, Suriyanarayanan N (2013) Synthesis and characterization of sprayed Zn-doped polycrystalline CuInS 2 thin films. Optik-International Journal for Light and Electron Optics 124:5089-5094.
[23] Lontchi J, Abaab M (2017) Study of structural, optical and electrical properties of thermal evaporated undoped and Na doped CuInS 2 thin films. Thin Solid Films 633:81-86.
[24] Huang F-Q, Liu M-L, Yang C (2011) Highly enhanced p-type electrical conduction in wide band gap Cu 1+ x Al 1− x S 2 polycrystals. Sol Energy Mater Sol Cells 95:2924-2927.
[25] Murali B, Krupanidhi S, Tailoring the Cu (In, Al) S 2 nanostructures for photonic applications, in: Photovoltaic Specialists Conference (PVSC), 2013 IEEE 39th, IEEE, 2013, pp. 2017-2022.
[26] Perng D-C, Kao T-T, Chang R-P (2014) Formation of wide band-gap CuInAlS 2 thin film and its application to UV Detectors. Thin Solid Films 572:28-32.
[27] Dhas CR, Venkatesh R, Kirubakaran DD, Merlin JP, Subramanian B, Raj AME (2017) Electrochemical sensing of glucose and photocatalytic performance of porous Co 3 O 4 films by nebulizer spray technique. Mater Chem Phys 186:561-573.
[28] Ma J, Shen W, Li C, Yu F (2015) Light reharvesting and enhanced efficiency of dye-sensitized solar cells based 3D-CNT/graphene counter electrodes. J Mater Chem A 3:12307-12313.
[29] Mane A, Moholkar A (2017) Effect of film thickness on NO 2 gas sensing properties of sprayed orthorhombic nanocrystalline V 2 O 5 thin films. Appl Surf Sci 416:511-520.
[30] Shinde V, Gujar T, Lokhande C (2007) LPG sensing properties of ZnO films prepared by spray pyrolysis method: effect of molarity of precursor solution. Sens Actuators B Chem 120:551-559.
[31] Dhas CR, Venkatesh R, Sivakumar R, Raj AME, Sanjeeviraja C (2017) Effect of solution molarity on optical dispersion energy parameters and electrochromic performance of Co3O4 films. Opt Mater 72:717-729.
[32] Moholkar A, Shinde S, Babar A, Sim K-U, Lee HK, Rajpure K, Patil P, Bhosale C, Kim J (2011) Synthesis and characterization of Cu 2 ZnSnS 4 thin films grown by PLD: solar cells. J Alloys Compd 509:7439-7446.
[33] Ravidhas C, Josephine AJ, Sudhagar P, Devadoss A, Terashima C, Nakata K, Fujishima A, Raj AME, Sanjeeviraja C (2015) Facile synthesis of nanostructured monoclinic bismuth vanadate by a co-precipitation method: structural, optical and photocatalytic properties. Mater Sci Semicond Process 30:343-351.
[34] Dhanam M, Kavitha B, Velumani S (2010) An investigation on silar Cu (In 1− x Al x) Se 2 thin films. Mater Sci Eng, B 174:209-215.
[35] Shabu R, Raj AME, Sanjeeviraja C, Ravidhas C (2015) Assessment of CuO thin films for its suitablity as window absorbing layer in solar cell fabrications. Mater Res Bull 68:1-8.
[36] Lopez-Otero A (1977) The dependence of the grain size of continuous epitaxial films on the growth conditions. J Cryst Growth 42:157-159.
[37] Dhas CR, Christy AJ, Venkatesh R, Anitha B, Josephine AJ, Kirubakaran DD, Arivukarasan D, Sudhagar P, Raj AME, Sanjeeviraja C (2017) CuInS2 Layer Deposition Through Nebulizer Spray Technique for Solar Cell Fabrication. Recent Trends in Materials Science and Applications 451-464.
[38] Li Y, Tan B, Wu Y (2006) Freestanding mesoporous quasi-single-crystalline Co3O4 nanowire arrays. J Am Chem Soc 128:14258-14259.
[39] Chen S-L, Tao J, Tao H-J, Shen Y-Z, Xu A-C, Cao F-X, Jiang J-J, Wang T, Pan L (2016) Rounded Cu 2 ZnSnS 4 nanosheet networks as a cost-effective counter electrode for high-efficiency dye-sensitized solar cells. Dalton Trans 45:4513-4517.
[40] Kumar V, Singh N, Mehra R, Kapoor A, Purohit L, Swart H (2013) Role of film thickness on the properties of ZnO thin films grown by sol-gel method. Thin Solid Films 539:161-165.

[41] Mahadik M, Shinde S, Mohite V, Kumbhar S, Rajpure K, Moholkar A, Bhosale C (2014) Photoelectrocatalytic activity of ferric oxide nanocatalyst: A synergestic effect of thickness. Ceram Int 40:9463-9471.
[42] Ho C-H (2011) Single crystal growth and characterization of copper aluminum indium disulfide chalcopyrites. J Cryst Growth 317:52-59.
[43] Perera SD, Zhang H, Ding X, Nelson A, Robinson RD (2015) Nanocluster seed-mediated synthesis of CuInS 2 quantum dots, nanodisks, nanorods, and doped Zn-CuInGaS 2 quantum dots. Journal of Materials Chemistry C 3:1044-1055.
[44] Sebastian T, Gopinath M, Sudha Kartha C, Vijayakumar KP, Abe T, Kashiwaba Y (2009) Role of substrate temperature in controlling properties of sprayed CuInS2 absorbers. Sol Energy 83:1683-1688.
[45] Ravi Dhas C, Christy AJ, Venkatesh R, Kirubakaran DD, Sivakumar R, Ravichandran K, Raj AME, Sanjeeviraja C (2017) Effect of sputtering power on properties and photovoltaic performance of CIGS thin film solar cells. Mater Res Innovations 21:286-293.
[46] Sivalingam K, Shankar P, Mani GK, Rayappan JBB (2014) Solvent volume driven ZnO nanopetals thin films: Spray pyrolysis. Mater Lett 134:47-50.
[47] Desai S, Suryawanshi M, Gaikwad M, Mane A, Kim J, Moholkar A (2017) Investigations on the thickness dependent structural, morphological, and optoelectronic properties of sprayed cadmium based transparent conducting oxide. Thin Solid Films 628:196-202.
[48] Boyraz C, Urfa Y (2015) Effect of solution molarity on microstructural and optical properties of CdCr 2 S 4 thin films. Mater Sci Semicond Process 36:1-6.
[49] Cheng K-W, Fan M-S (2013) Preparation and characterization of CuIn x Al 1− x S 2 films using the sulfurization of metal precursors for photoelectrochemical applications. J Taiwan Inst Chem Eng 44:407-414.
[50] Cao H, Pei Z, Gong J, Sun C, Huang R, Wen L (2004) Transparent conductive Al and Mn doped ZnO thin films prepared by DC reactive magnetron sputtering. Surf Coat Technol 184:84-92.
[51] Kavitha B, Dhanam M (2013) Transport properties of copper indium aluminum selenide thin films deposited by successive Ionic layer adsorption and reaction. Mater Sci Semicond Process 16:495-503.
[52] Nagarajan S, Sudhagar P, Raman V, Cho W, Dhathathreyan K, Kang YS (2013) A PEDOT-reinforced exfoliated graphite composite as a Pt-and TCO-free flexible counter electrode for polymer electrolyte dye-sensitized solar cells. J Mater Chem A 1:1048-1054.
[53] Burschka J, Brault V, Ahmad S, Breau L, Nazeeruddin MK, Marsan B, Zakeeruddin SM, Grätzel M (2012) Influence of the counter electrode on the photovoltaic performance of dye-sensitized solar cells using a disulfide/thiolate redox electrolyte. Energy Environ Sci 5:6089-6097.
[54] Chen S, Xu A, Tao J, Tao H, Shen Y, Zhu L, Jiang J, Wang T, Pan L (2015) In-Situ and Green Method To Prepare Pt-Free Cu2ZnSnS4 (CZTS) Counter Electrodes for Efficient and Low Cost Dye-Sensitized Solar Cells. ACS Sustainable Chem Eng 3:2652-2659.
[55] Swami SK, Chaturvedi N, Kumar A, Chander N, Dutta V, Kumar DK, Ivaturi A, Senthilarasu S, Upadhyaya HM (2014) Spray deposited copper zinc tin sulphide (Cu 2 ZnSnS 4) film as a counter electrode in dye sensitized solar cells. Phys Chem Chem Phys 16:23993-23999.
[56] Wu M, Lin X, Hagfeldt A, Ma T (2011) Low-Cost Molybdenum Carbide and Tungsten Carbide Counter Electrodes for Dye-Sensitized Solar Cells. Angew Chem Int Ed 50:3520-3524.
[57] Bai L, Ding J, Yuan N, Hu H, Li Y, Fang X (2013) Cu 2 ZnSnS 4/graphene composites as low-Cost counter electrode materials for dye-Sensitized solar cells. Mater Lett 112:219-222.

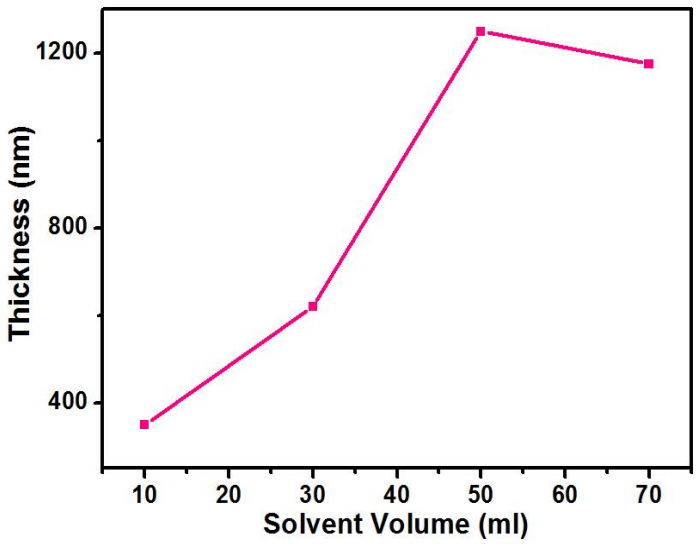

Figure 1: Solvent volume vs thickness of CIAS thin films

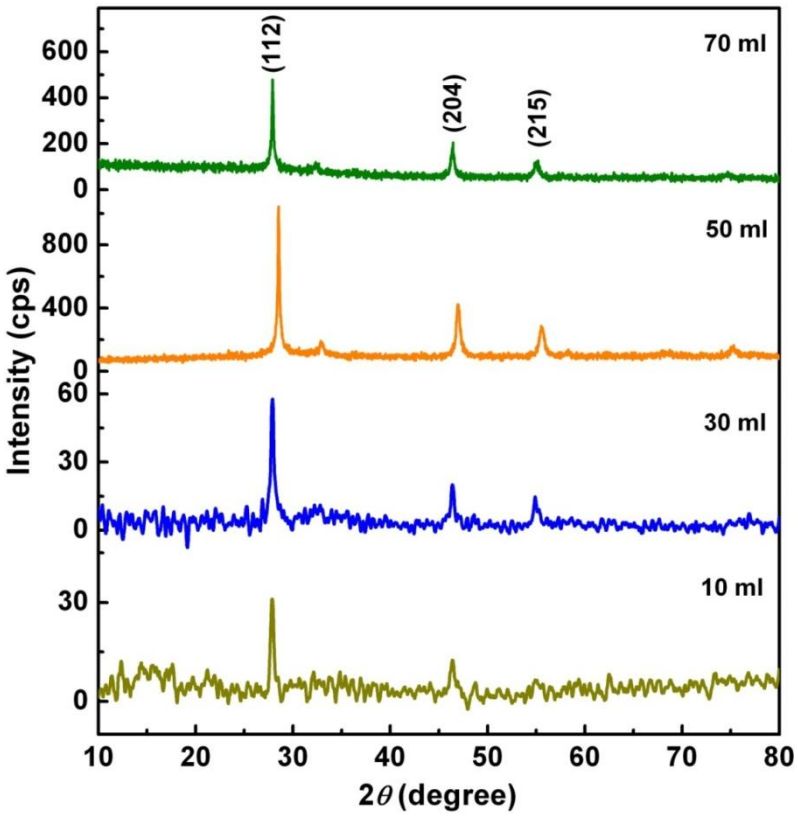

Figure 2: X-ray diffraction of CIAS thin films for different solvent volumes

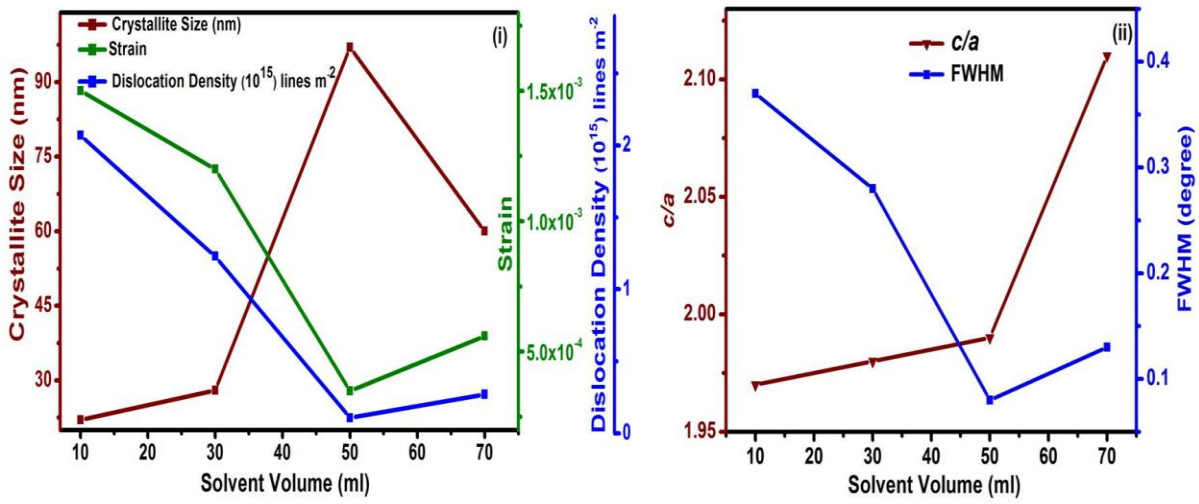

Figure 3 (i) Solvent volume vs crystallite size, strain and dislocation density and (ii) Solvent volume vs tetragonal c/a ratio and FWHM of CIAS thin films

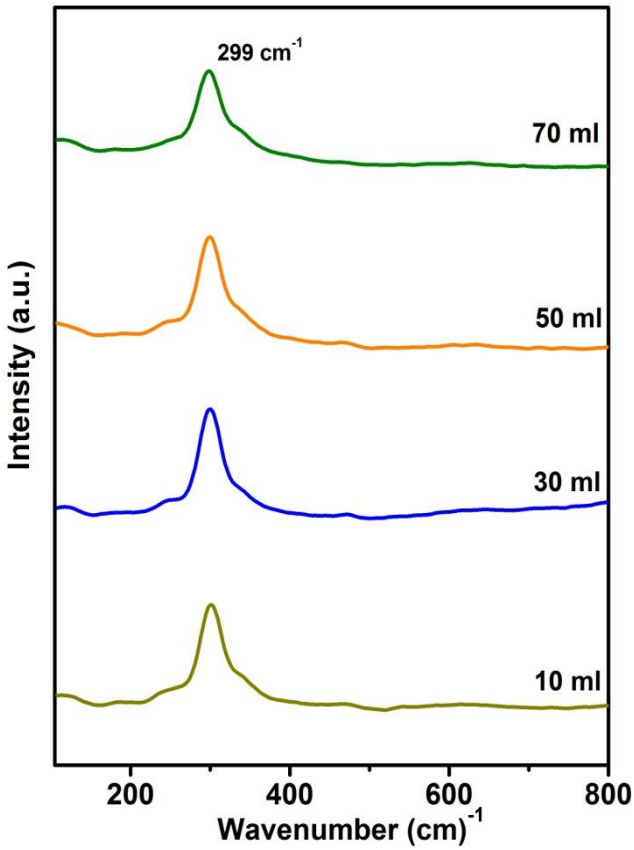

Figure 4: Raman Spectra of CIAS thin films for different solvent volumes

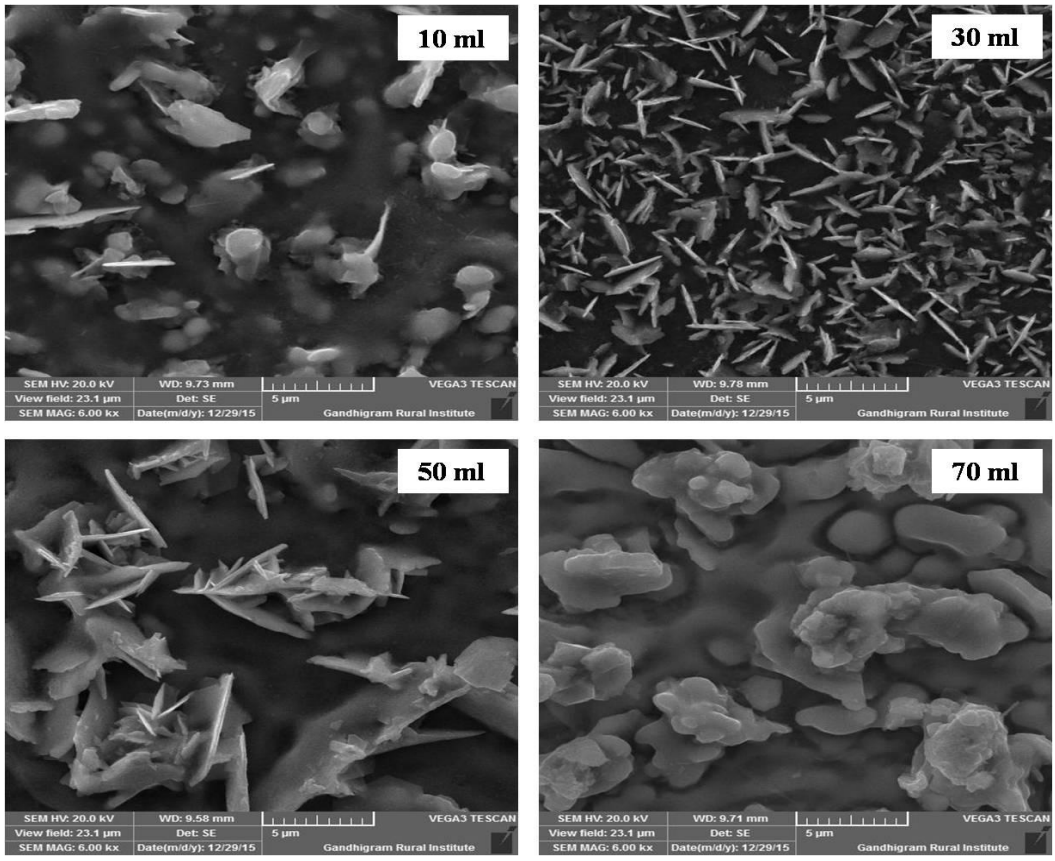

Figure 5: SEM images of CIAS thin films for different solvent volumes

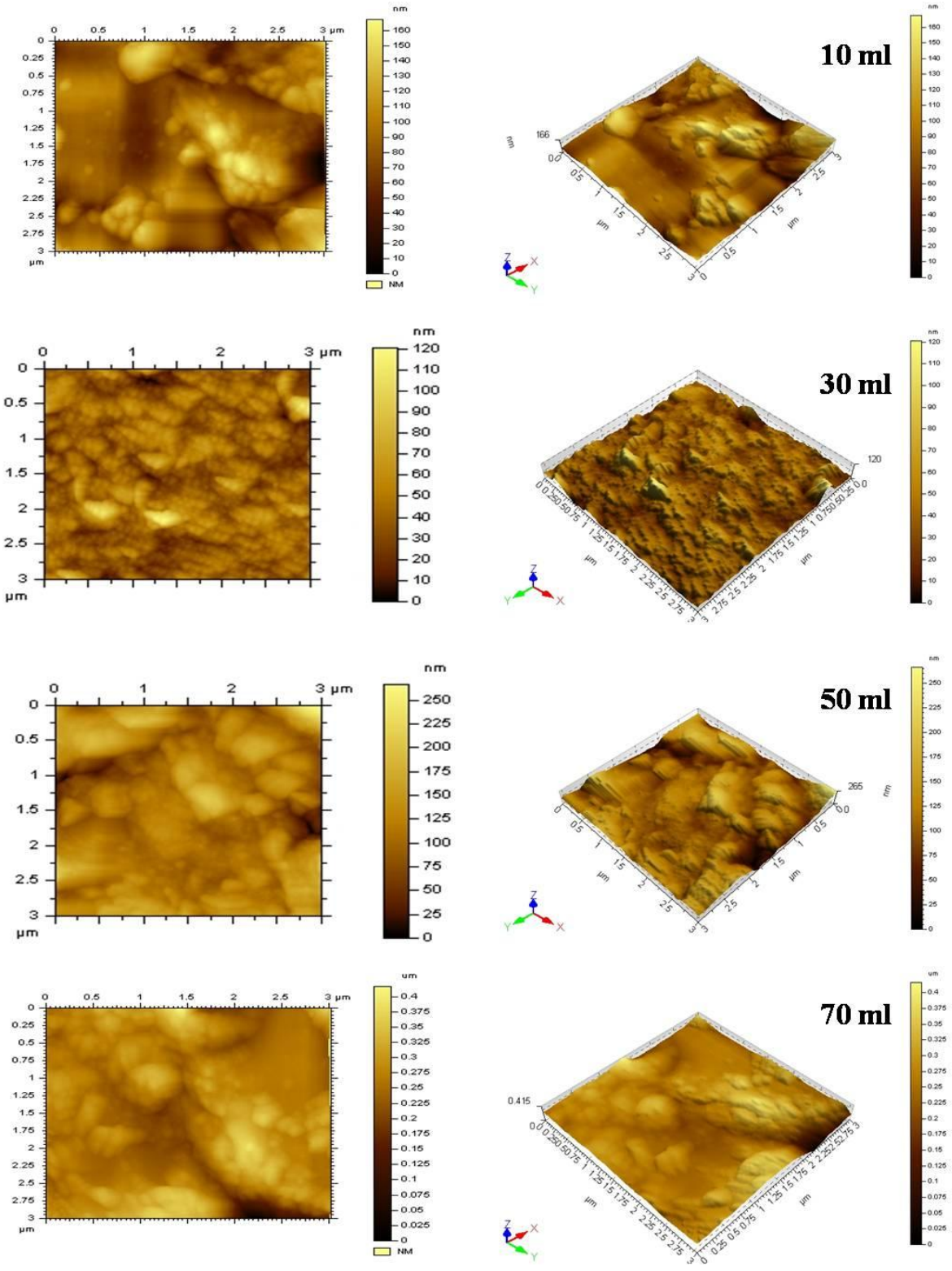

Figure 6: AFM images of CIAS thin films for different solvent volumes

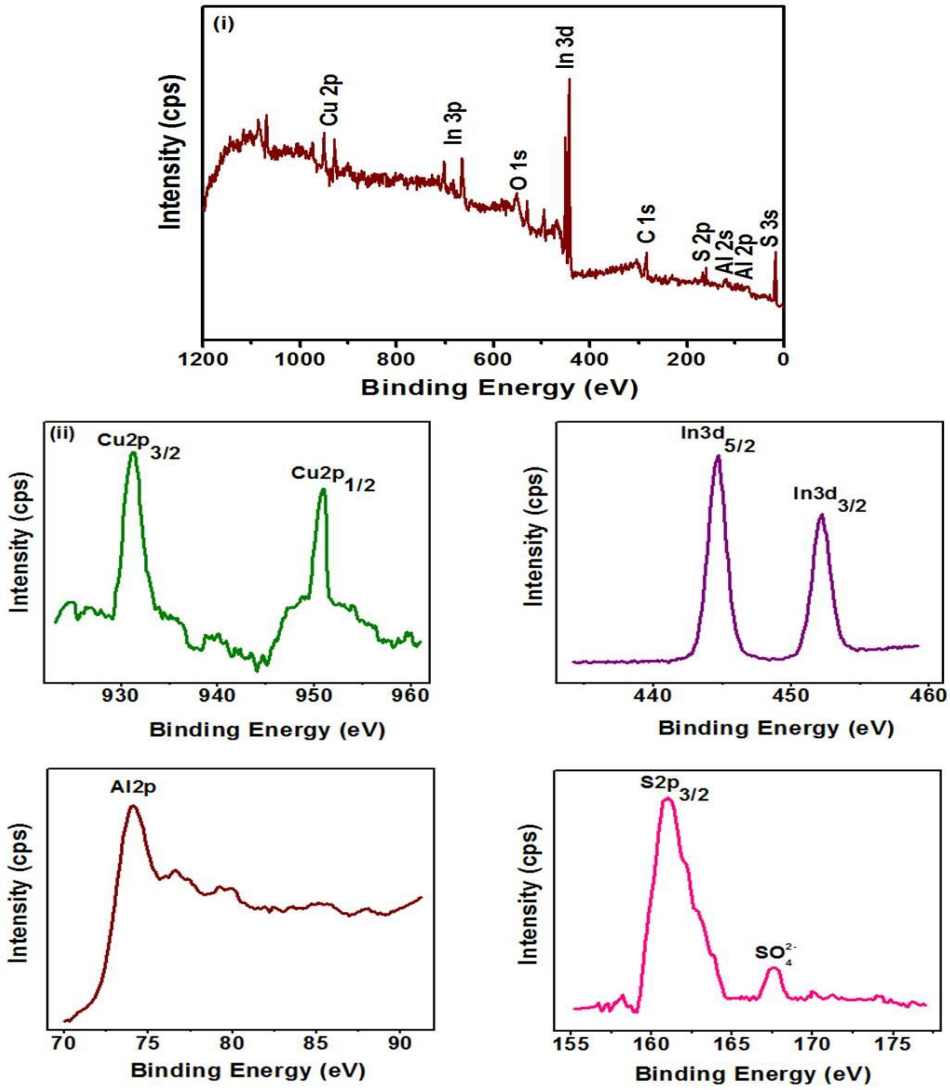

Figure 7: (i) Survey spectrum and (ii) Core level spectra of Cu, In, Al and S of CIAS thin film deposited by 50 ml solvent volume

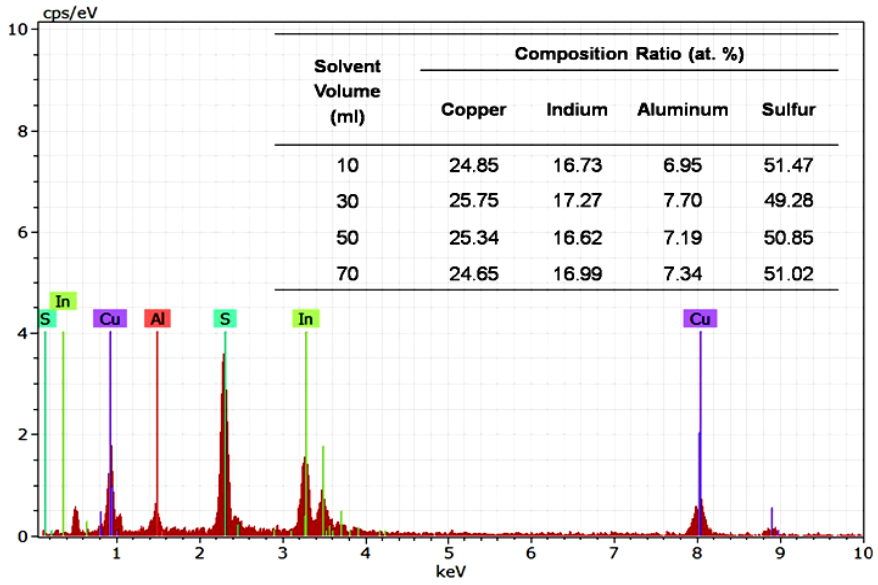

Solvent Volume (ml)	Composition Ratio (at. %)			
	Copper	Indium	Aluminum	Sulfur
10	24.85	16.73	6.95	51.47
30	25.75	17.27	7.70	49.28
50	25.34	16.62	7.19	50.85
70	24.65	16.99	7.34	51.02

Figure 8: Energy Dispersive X-ray Analysis spectra of CIAS thin film

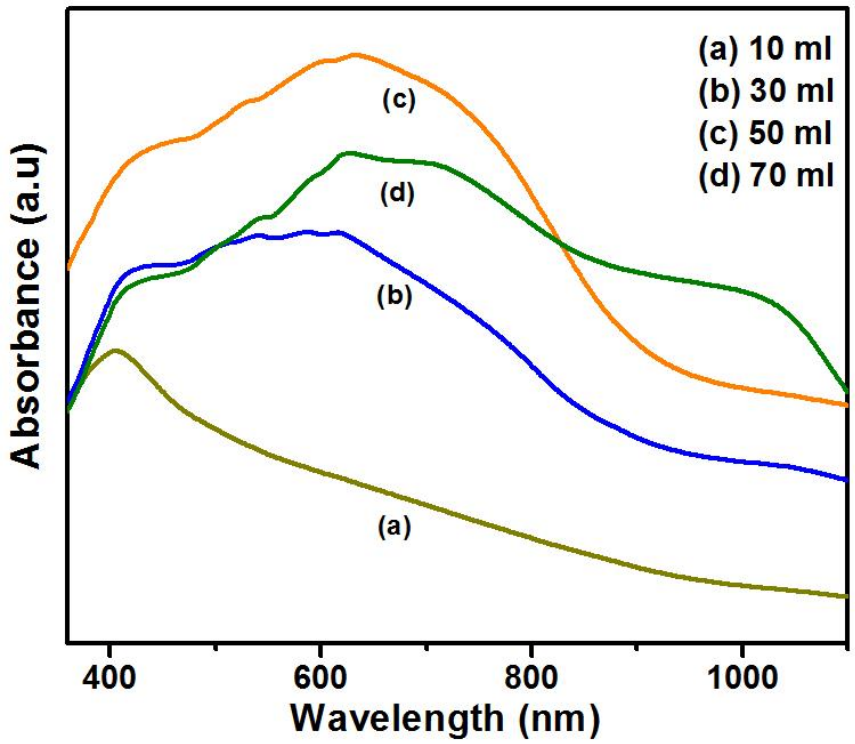

Figure 9: Absorbance vs wavelength of CIAS thin films for different solvent volumes

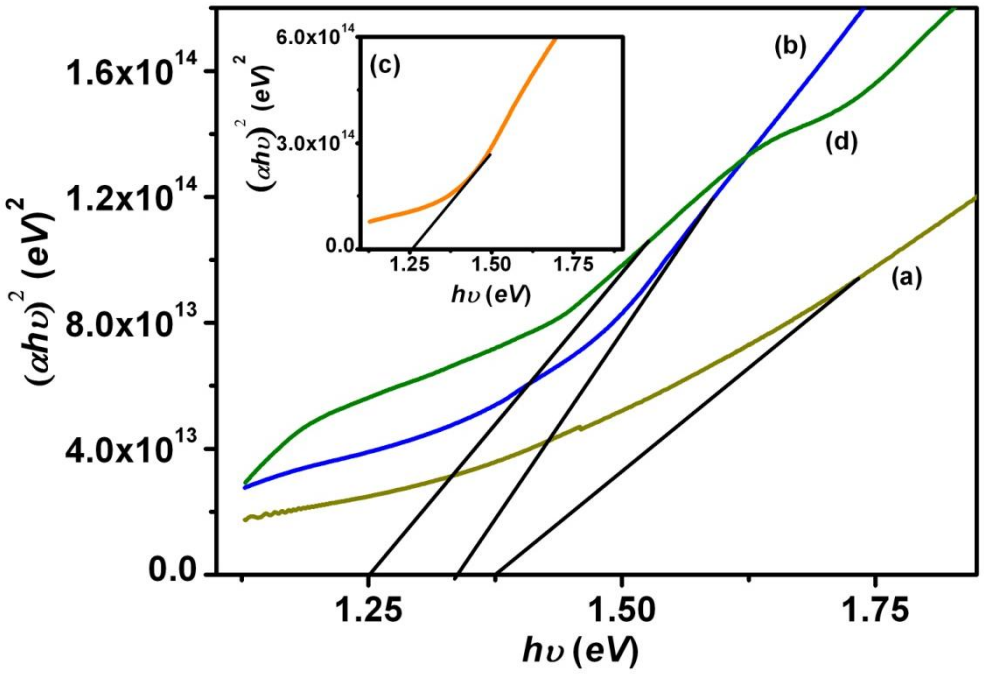

Figure 10: Optical band gap of CIAS thin films for different solvent volumes

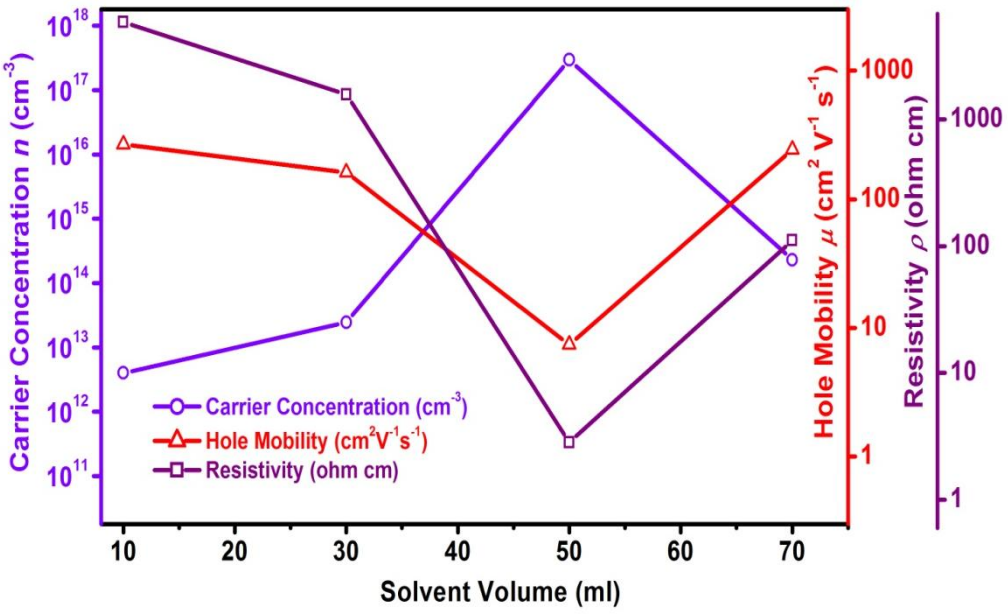

Figure 11: Electrical parameters of CIAS thin films for different solvent volumes

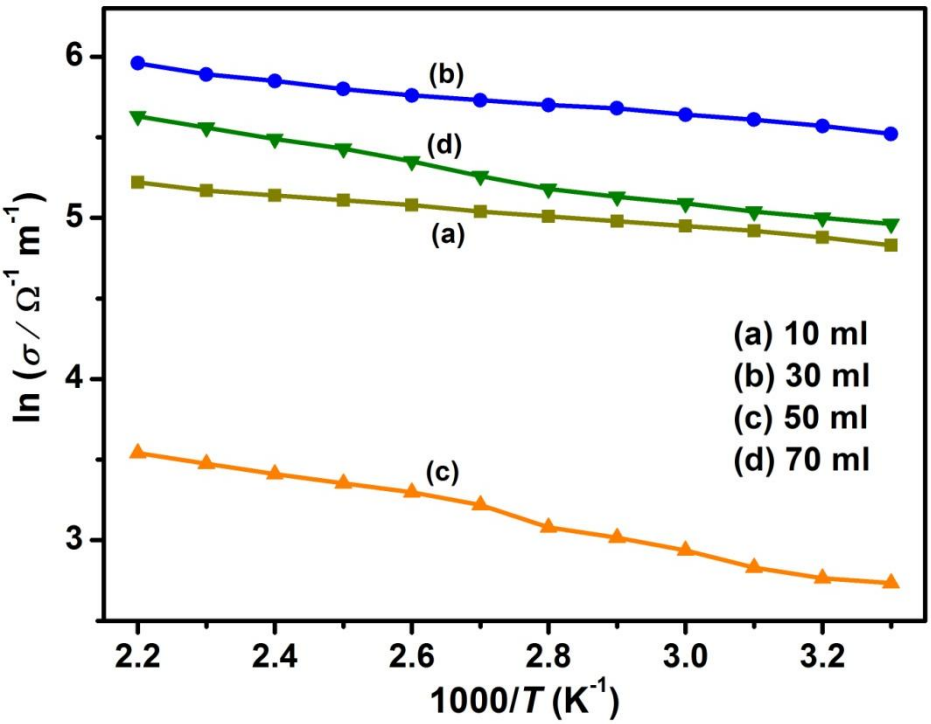

Figure 12: Arrhenius plot (ln σ vs. 1000/T (K^{-1})) of CIAS films for different solvent volumes

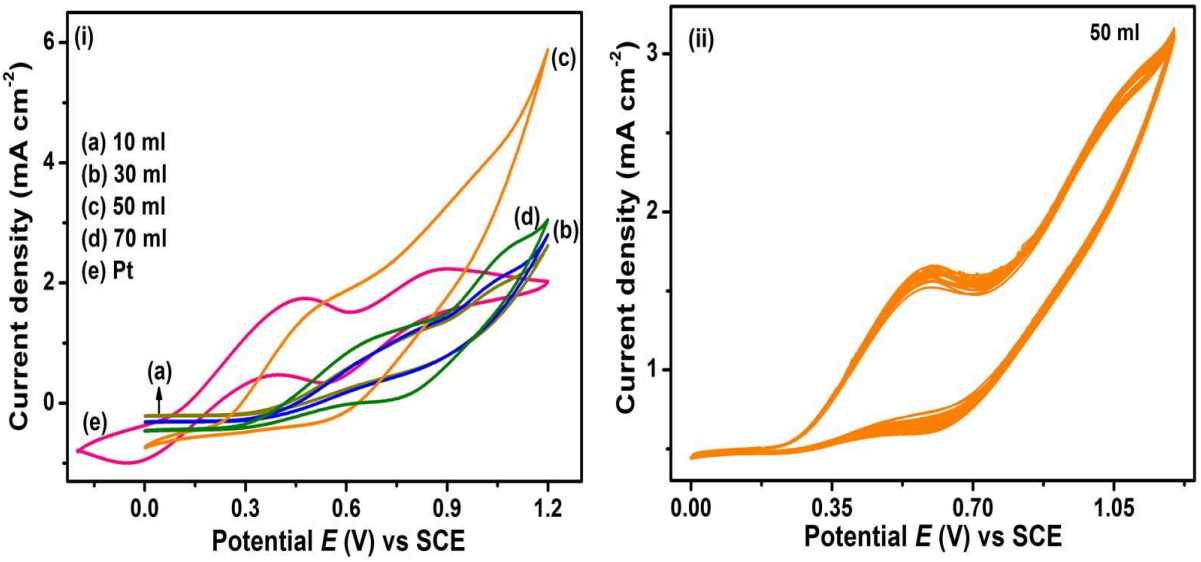

Figure 13: (i) Cyclic voltammograms of Pt and CIAS CEs and (ii) 40 continuous cyclic voltammograms of CIAS CE deposited for 50 ml

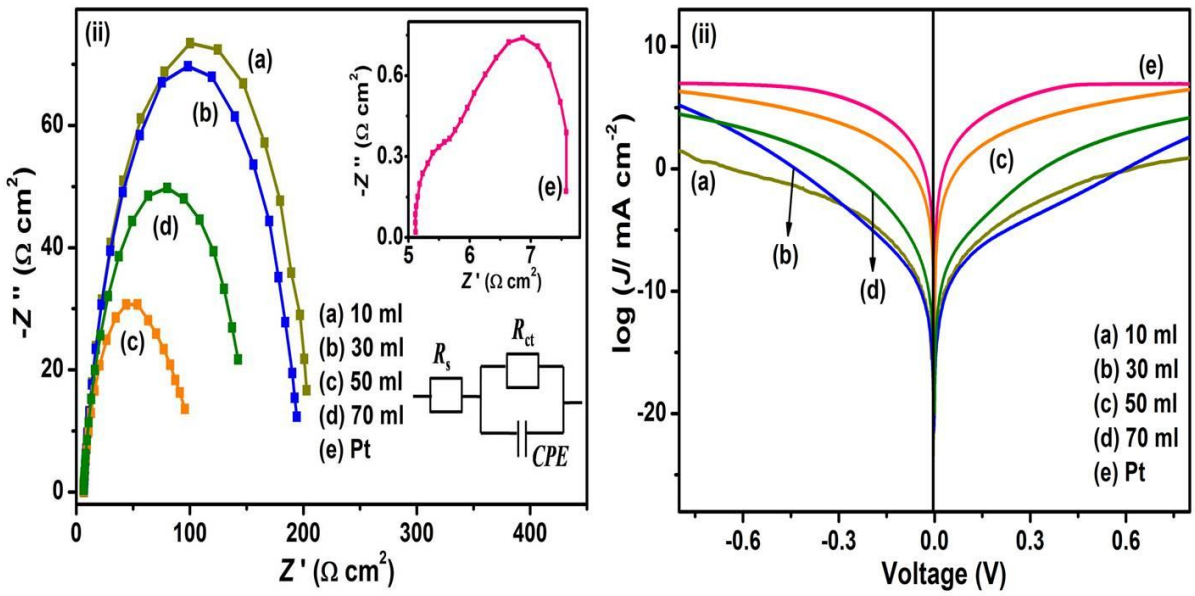

Figure 14: (i) EIS spectra of the TiO_2 based DSSCs devices with Pt and CIAS CEs and (ii) Tafel polarization curves of Pt and CIAS symmetric cells

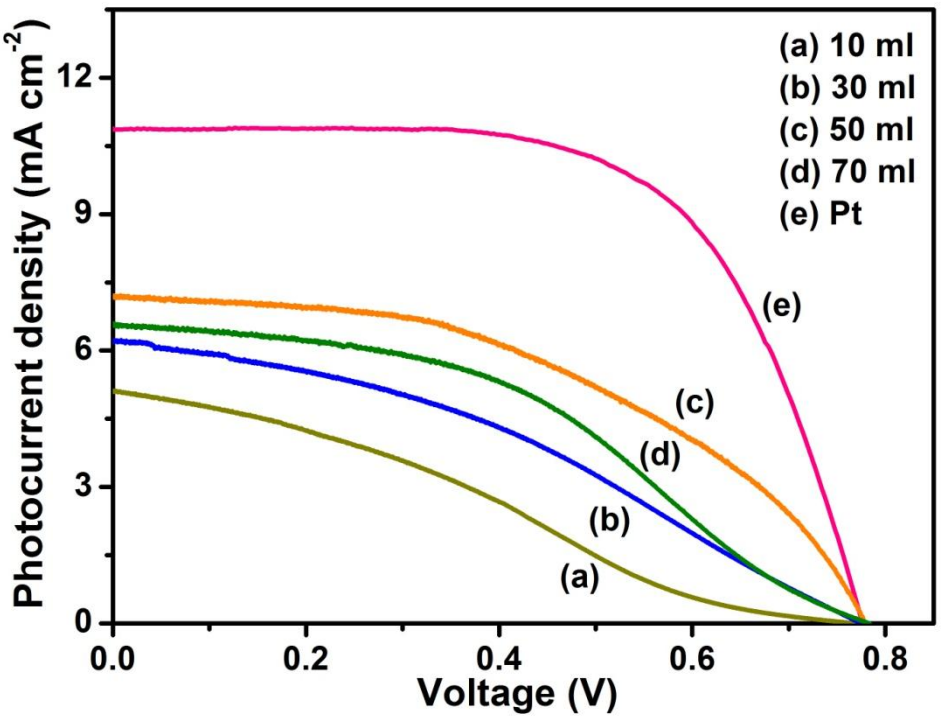

Figure 15: *J – V* characteristics of DSSCs with Pt and different CIAS CEs

Table 1: Lattice Constants, Root Mean Square Roughness and Activation Energy of CIAS thin films

Solvent Volume (ml)	Lattice Constants (Å)		Root Mean Square Roughness (nm)	Activation Energy (eV)
	a	***c***		
10	5.57	11.01	41.4	0.06
30	5.55	11.04	24.8	0.07
50	5.54	11.05	23.3	0.19
70	5.32	11.27	23.9	0.11

Table 2: Electrochemical parameters of DSSCs for different CEs

Samples	J_{pa} (mA cm^{-2})	J_{pc} (mA cm^{-2})	ΔE_p (mV)	R_s (Ω cm^2)	R_{ct} (Ω cm^2)	log J_{lim} (mA cm^{-2})
Pt	1.75	-1.00	421	5.12	2.46	7.14
10 ml	1.04	-0.22	484	6.80	196.19	0.92
30 ml	1.12	-0.29	465	6.63	187.68	2.50
50 ml	1.63	-0.57	331	6.14	89.50	6.42
70 ml	1.17	-0.38	439	6.45	136.13	4.09

Table 3: Photocurrent density-voltage (J-V) parameters of DSSCs for different CEs

Samples	V_{oc} (V)	J_{sc} (mA cm^{-2})	*FF*	η (%)
Pt	0.78	10.87	0.63	5.30
10 ml	0.76	5.11	0.29	1.14
30 ml	0.77	6.21	0.35	1.69
50 ml	0.78	7.22	0.45	2.55
70 ml	0.78	6.56	0.42	2.12